Nano Research 2017, 10(2): 381–396
DOI 10.1007/s12274-016-1298-0
Research Article
ISSN 1998-0124
CN 11-5974/O4

Rambutan-like hierarchically heterostructured CeO_2-CuO hollow microspheres: Facile hydrothermal synthesis and applications

Yongjun Ji[1,§] (✉), Zheying Jin[1,§], Jing Li[1,2], Yu Zhang[1,2], Hezhi Liu[1], Laishun Shi[3], Ziyi Zhong[4,5], and Fabing Su[1] (✉)

[1] *State Key Laboratory of Multiphase Complex Systems, Institute of Process Engineering, Chinese Academy of Sciences, Beijing 100190, China*
[2] *University of Chinese Academy of Sciences, Beijing 100049, China*
[3] *School of Chemistry and Chemical Engineering, Shandong University, Jinan 250100, China*
[4] *Institute of Chemical Engineering and Sciences, 1 Pesek Road, Jurong Island, Singapore 627833, Singapore*
[5] *School of Chemical & Biomedical Engineering, Nanyang Technological University (NTU), 62 Nanyang Drive, Singapore 637459, Singapore*
[§] *These authors contributed equally to this work.*

Received: 27 July 2016
Revised: 20 September 2016
Accepted: 23 September 2016

KEYWORDS
heterostructure, hollow sphere, rambutan, supercapacitors, Rochow reaction

ABSTRACT

Hierarchically heterostructured hollow spheres are of great interest for a wide range of applications owing to their unique structural features and properties. However, the fabrication of well-defined hollow spheres with highly specific morphology for mixed transition metal oxides on a large scale remains challenging. In this work, uniform rambutan-like heterostructured CeO_2-CuO hollow microspheres with numerous copper–ceria interfacial sites and nanorods and nanoparticles as building blocks are prepared via a facile hydrothermal method followed by calcination. Importantly, this approach can be readily scaled up and is applicable to the synthesis of various CuO-based mixed metal oxide complex hollow spheres. The as-prepared CeO_2-CuO hollow rambutans exhibit superior performance both as electrode materials for supercapacitors and as Cu-based catalysts for the Rochow reaction, mainly due to the small primary nanoparticle constituents, high surface area, and formation of numerous interior heterostructures.

1 Introduction

In principle, hollow micro- and nanostructures can possess very high specific surface areas and atomic utilization efficiencies, having promising applications in catalysis, sensors, pollution treatment, energy storage, encapsulation, and controllable release of drugs [1–10]. Various approaches, including reverse micelle transitions, sol–gel processes, templating methods, and electrochemical deposition have been developed

Address correspondence to Yongjun Ji, yjji@ipe.ac.cn; Fabing Su, fbsu@ipe.ac.cn

to controllably prepare different hollow structures [11–13]. Among these, templating methods have been demonstrated to be very effective. However, this approach requires complicated and tedious procedures such as coating of the desired materials on the surface of the preforming templates and subsequent template removal to generate hollow structures, which undoubtedly increases the synthesis cost and makes it not economical [14, 15]. Furthermore, the hollow structures are often partially damaged during the template removal process, which limits the large-scale application of this method. Recently, the approach of self-assembling nanostructured building blocks into hollow structures has attracted much attention, exhibiting a high potential for the generation of hollow micro- and nanostructures [16–18]. In this synthetic approach, various organic solvents and/or surfactants are employed to control the product morphology. For instance, Yao et al. have prepared multi-shelled Co_3O_4 hollow spheres by assembling Co_3O_4 nanosheets in an ethylene glycol (EG)-based system containing poly(vinylpyrrolidone) (PVP) [19]. Furthermore, Lou et al. have reported the construction of Fe_3O_4 hierarchical hollow microspheres from *in situ* formed Fe_3O_4 nanoplate building blocks in the presence of EG and ethylenediamine (EDA) [20]. Very recently, Lou et al. have also organized ultrathin nanosheets into Fe_3O_4 hollow spheres using a solvent mixture containing glycerol, isopropyl alcohol (IPA), and a small amount of water [21]. However, the striking feature of most of these hollow structures is that they are generally composed of a single oxide component. Multicomponent metal oxides have attracted attention for their potential use in catalysis, photocatalysis, and energy transfer applications due to their unique chemical and physical properties [22, 23]. Furthermore, recent reports show that multi-component heterostructured metal oxides usually display interesting synergistic effects between their components, which are helpful to enhance performance (e.g., electrochemical or catalytic performance) [24, 25]. However, to our knowledge, no successful example of controllable, facile, and large-scale synthesis of hierarchical hollow heterostructures containing multiple metal oxide components with specific morphology is described in literature.

In this study, an inverse CeO_2-CuO system (CuO acting as a support for CeO_2) was chosen as a research object, since it is considered an economically very promising candidate for the preferential oxidation of CO (CO-PROX) in H_2-rich streams, which is a key reaction for the practical use of H_2 in proton-exchange membrane fuel cells (PEMFCs), with CO being highly poisonous to the electrocatalyst [26–28]. Herein, we report a simple one-pot template-free hydrothermal approach followed by calcination to the synthesis of bi-component heterostructured CeO_2-CuO hollow microspheres possessing unique rambutan-like morphology and an increased number of copper–ceria interfacial sites. Detailed investigation reveals an interesting structure evolution process: 1) The initially formed CuO nanoparticles are first aggregated to form solid CuO microspheres; 2) the newly generated CeO_2 nanospheres are deposited on the CuO microspheres; 3) the inside-out Ostwald ripening process takes place, resulting in the formation of a yolk–shell structure; 4) eventually, well-defined hollow microspheres are formed, accompanied by the growth of *in situ* formed nanosheets on their surface. In this synthesis, the product internal structure can be simply tuned by controlling the reaction time. Importantly, pure water was used as a solvent, making the process much greener and more economical. Furthermore, the production can be easily scaled up to a multi-gram scale and is potentially applicable to other systems. Owing to their unique structural features, the as-prepared CeO_2-CuO hollow heterostructures not only showed superior electrochemical performance as electrode materials for supercapacitors, but also exhibited enhanced catalytic activity and stability as a catalyst for the Rochow reaction.

2 Experimental

2.1 Material synthesis

All chemicals used were of analytical grade, including copper (II) acetate monohydrate ($Cu(CH_3COO)_2{\cdot}H_2O$), cerium (III) acetate ($Ce(CH_3COO)_3$), and sodium carbonate (Na_2CO_3). These reagents were purchased from Sinopharm Chemical Reagent Co. Ltd., China and were used as received. The precursor particles were synthesized by a facile hydrothermal method in

absence of any template or surfactant. In a typical synthesis, $Cu(CH_3COO)_2{\cdot}H_2O$ (1.200 g, 6 mmol) and $Ce(CH_3COO)_3$ (0.095 g, 0.3 mmol) were dissolved in deionized water (60.0 mL) under vigorous stirring, followed by the dropwise addition of a 0.3 M Na_2CO_3 solution (20.0 mL). The obtained mixture was transferred into a 100-mL Teflon-lined stainless steel autoclave and kept in an oven at 60–180 ℃ for 0.5–18 h. After cooling down to room temperature, the resulting product was filtered, washed with 3 × deionized water and ethanol, and dried at 60 ℃ in air for 8 h. Finally, the as-synthesized intermediate was converted into CeO_2-CuO by calcination at 400 ℃ for 3 h in air. The syntheses of pure CuO and CeO_2 followed similar procedures, with only $Cu(CH_3COO)_2{\cdot}H_2O$ or $Ce(CH_3COO)_3$ added, respectively.

2.2 Characterization

Powder X-ray diffraction (XRD) patterns were recorded on a PANalytica X'Pert PRO MPD instrument using Cu Kα radiation (λ = 1.5418 Å) and were compared with the respective card number of the Joint Committee on Powder Diffraction Standards (JCPDS). The sample dimensions, morphologies, and crystal lattices were characterized by field-emission scanning electron microscopy (FESEM; JEM-6700F, JEOL, Japan) and transmission electron microscopy (TEM; JEM-2010F, JEOL, Tokyo, Japan), as well as cold field-emission spherical-aberration-corrected TEM (Cold FEG Cs-corrected TEM; JEM-ARM200F, Japan) operated at an accelerating voltage of 200 kV. The surface chemical composition was determined by X-ray photoelectron spectroscopy (XPS) (Model VG ESCALAB 250 spectrometer, Thermo Electron, UK) using a non-monochromatized Al Kα X-ray source (1,486.6 eV). N_2 adsorption at −196 ℃ was measured using a Quantachrome surface area and pore size analyzer (NOVA 3200e). Prior to the measurement, the sample was degassed under vacuum at 200 ℃ for 3 h. The specific surface areas were measured according to the Brunauer–Emmett–Teller (BET) method in the relative pressure range of 0.05–0.2. UV–vis absorption spectra were recorded at room temperature using a UV-vis absorption spectrometer (Shimadzu). The micro-Raman spectra are measured at room temperature using LABRAM HR 800 model (In via laser Raman microscope) with a 632 nm excitation source of a He–Ne laser with the power of 17 mW. Elemental analysis was performed using an inductively coupled plasma optical emission spectrometer (ICP-OES; Optima 5300DV, Perkin Elmer, USA).

2.3 Electrochemical measurements

The electrochemical tests were conducted in aqueous KOH electrolyte (6.0 M) using a CHI 660D electrochemical workstation and a three-electrode cell, with Pt foil as the counter electrode and a standard calomel electrode (SCE) as the reference electrode. The nominal area of all samples immersed into the electrolyte was controlled to be around 1 cm × 1 cm. The mass loading of all samples was ca. 1.2 mg·cm^{-2}.

2.4 Catalyst evaluation

Catalyst evaluation was performed in a fixed-bed quartz reactor. Si powder (10.0 g, 20–50 mesh, provided by Jiangsu Hongda New Material Co., Ltd.), catalyst (0.2 g), and zinc promoter (0.02 g, A.R., Sinopharm Chemical Reagent Co., Ltd.) were homogeneously mixed to form a contact mass, which was loaded in the reactor. The reactor was purged with purified N_2 for 0.5 h, followed by heating to 325 ℃ within 1 h under a flow of N_2 (25 mL·min^{-1}). Subsequently, the N_2 flow was stopped, and MeCl gas was introduced into the reactor at a flow rate of 25 mL·min^{-1} to react with Si. The reaction was stopped after 24 h, and the gaseous product was condensed at –5 ℃ in a circulator bath controlled by a programmable thermal circulator (GDH series, Ningbo Xinzhi Biological Technology Co., Ltd., China). Gas chromatography/mass spectrometry (GC-MS) (QP2010, Shimadzu) was used for the identification of products, which mainly comprised methyltrichlorosilane (CH_3SiCl_3, M1), dimethyldichlorosilane ($(CH_3)_2SiCl_2$, M2), trimethylchlorosilane ($(CH_3)_3SiCl$, M3), methyldichlorosilane (CH_3SiHCl_2, M1H), dimethylchlorosilane ($(CH_3)_2SiHCl$, M2H), low boilers (LBs), and high boilers (HBs). The products in the liquid solution were quantitatively analyzed by gas chromatography (Agilent-7890A, KB-210 capillary column, thermal conducting detector). The mass fraction of a given product (with respect to the total product mass) was defined as its selectivity. The waste contact mass (residual solid after reaction) containing unreacted Si powder, Cu compounds, and

promoters was weighed to calculate the conversion of Si, which was defined as the contact mass weight difference before and after the reaction divided by the weight of Si before the reaction, as expressed as the following formula

$$\text{Conversion of Si } (C_{si}) = \frac{\text{Weight (contact mass before reaction)} - \text{weight (contact mass after reaction)}}{\text{Weight (Si before reaction)}} \times 100\%$$

3 Results and discussion

3.1 Characterization of CeO_2-CuO hollow microspheres

The hollow CeO_2-CuO rambutans were prepared by a facile hydrothermal reaction followed by calcination, using $Cu(CH_3COO)_2 \cdot H_2O$ and $Ce(CH_3COO)_3$ as precursors (more details in the Experimental Section). Figure 1(a) shows the crystal phase of the calcined product analyzed by powder XRD. The diffraction peaks could be indexed to monoclinic CuO (JCPDS No. 01-089-5898) and face-centered cubic (fcc) CeO_2 (JCPDS No. 03-065-5923), with Scherrer analysis of the $\{\bar{1}11\}$ peak indicating grain sizes of about 28 nm for CuO. No traces of other impurities such as Cu_2O, $Cu_2(OH)_2CO_3$, or $(CeOH)CO_3$ were observed. The morphology of the as-obtained phase-pure CeO_2-CuO was examined by FESEM. Low-magnification FESEM imaging showed that the as-prepared products exhibited rambutan-like morphology, with the prickly CuO microspheres having an average size of ca. 5 μm, while that of the smooth CeO_2 spheres ranged from 400 to 500 nm. These spheres were tightly embedded in the surface of the CuO microspheres (Figs. 1(b) and 1(c)). More detailed characterization results are presented in Fig. S1 (in the Electronic Supplementary Material (ESM)), which shows that all obtained products were uniform in size. A nearly 95% morphological

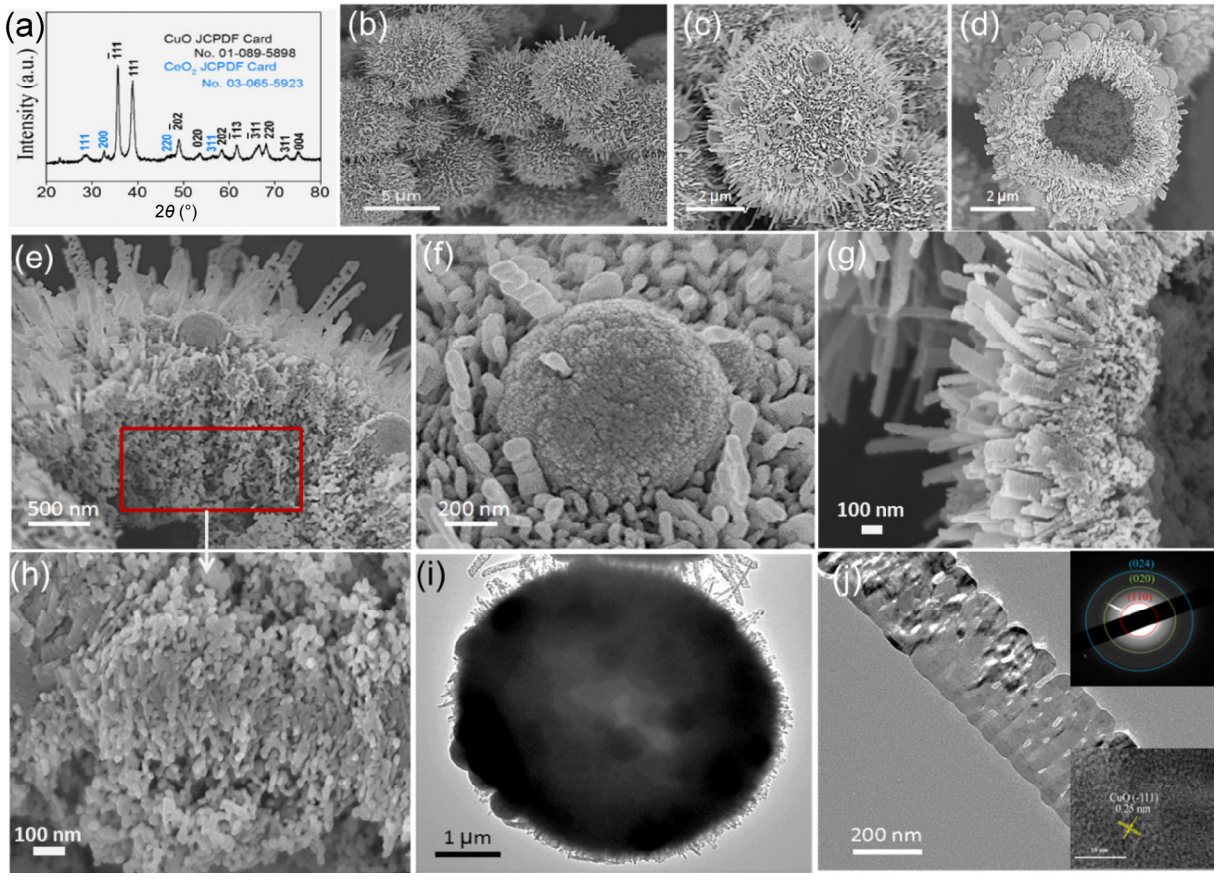

Figure 1 (a) XRD pattern, (b)–(h) FESEM images, (i) and (j) TEM images of the as-obtained CeO_2-CuO hollow microspheres. The inset of panel (j) (top right) shows the corresponding SAED pattern, with the HRTEM image of CuO nanosheets shown at the bottom right.

yield of the above type was achieved, together with a 94% product yield. Crushed microspheres (Fig. 1(d) and Fig. S1(b) in the ESM) clearly demonstrated that the "rambutan" exhibited a cavity and was coreless. As shown in Fig. S1(c) (in the ESM), the CuO shell thickness was estimated as ca. 1 μm. A close observation of the magnified images revealed that the spherical CeO_2 was composed of small nanoparticles, while the CuO spherical shell was constructed from interconnected disordered nanoparticles and nanorods assembled from the primary nanoparticle building units (Figs. 1(e)–1(h)). The nanorods were about 100 nm wide and 200 nm long, while the primary nanoparticles were typically about 30 nm in size. In addition, these nanorods aligned with each other on a nanoparticle layer along some main crystallographic axes of CuO via "oriented attachment", pointing to the center of the sphere, as displayed in Fig. 1(f). Interestingly, a large amount of porous nanosheets was grown on the microsphere surface, being intertwined with each other. The well-defined hollow structure was further verified by TEM imaging (Fig. 1(i)), which shows an obvious contrast between the dark edge and the pale center. Epitaxial porous nanosheets with a thickness of ca. 20 nm are clearly visible in the magnified TEM image (Fig. 1(j)). Furthermore, the selected area electron diffraction (SAED) pattern (inset in Fig. 1(j)) of the porous nanosheets confirmed the highly polycrystalline nature of CuO. High-resolution transmission electron microscopy (HRTEM) analysis verified the interplanar spacing of 0.25 nm, which was assigned to the $(\bar{1}11)$ plane of monoclinic CuO. To further study the local microstructure of the hollow spheres, spherical aberration-corrected scanning transmission electron microscopy (STEM) techniques were used. High-angle annular dark-field (HAADF)-STEM imaging directly confirmed that the CeO_2 spheres were composed of random nanoparticles with sizes of about 2 nm (Figs. 2(a) and 2(b)), and atomic-resolution HAADF-STEM imaging (Fig. 2(c)) clearly showed the (200) facets

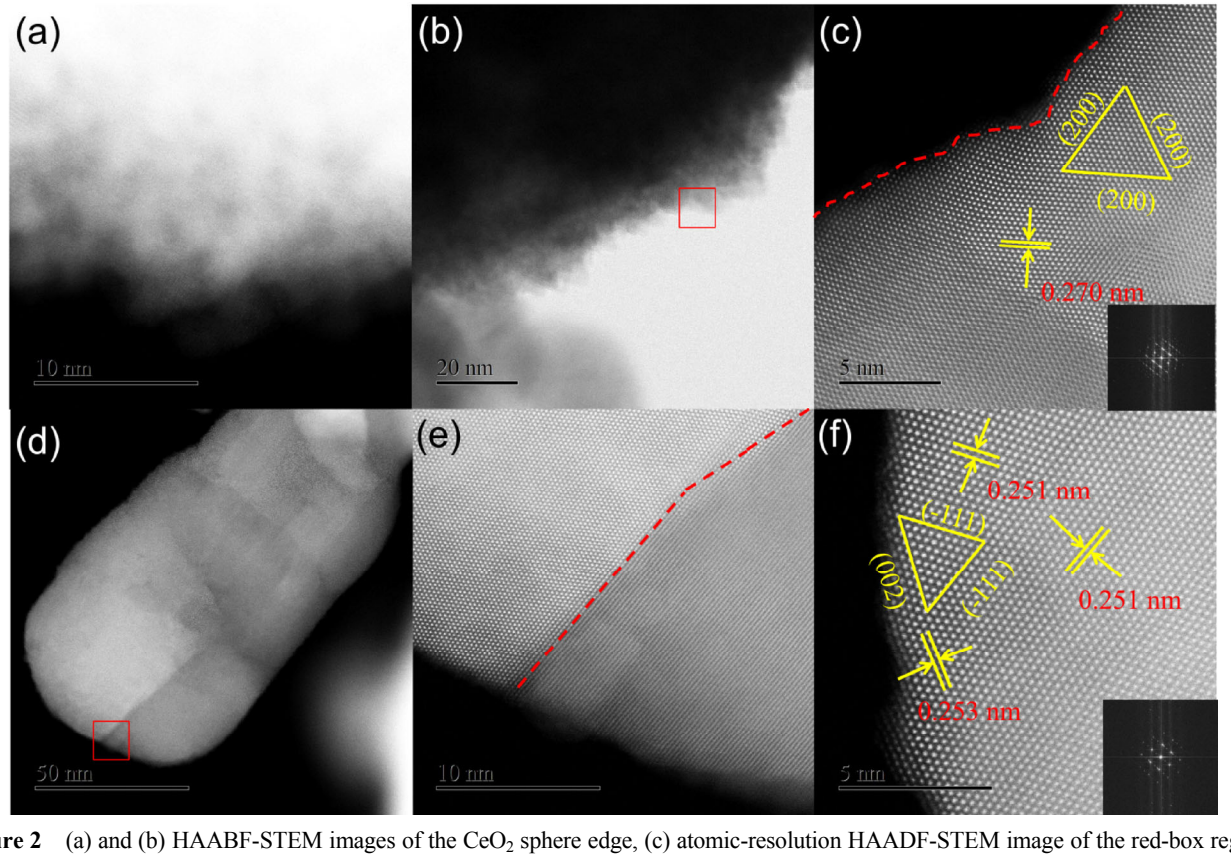

Figure 2 (a) and (b) HAABF-STEM images of the CeO_2 sphere edge, (c) atomic-resolution HAADF-STEM image of the red-box region in (b) (bottom inset shows the corresponding FFT pattern), (d) HAADF-STEM image of a CuO nanorod, (e) and (f) atomic-resolution HAADF-STEM images of the red-box region in (d) (bottom inset in (f) shows the corresponding FFT pattern).

of the fcc CeO_2. The CuO nanorods were further confirmed to be composed of nanoparticles with clearly observed junctions (Figs. 2(d) and 2(e)). The lattice spacing of 0.251 nm shown in Fig. 2(f) was assigned to the $(\bar{1}11)$ or (002) plane of monoclinic CuO. It should be noted that the surface was quite rough, with numerous atomic steps/corners present (as indicated by the dotted line in Figs. 2(c) and 2(e)), which should impact their catalytic activity. The bonding between the interconnected primary building units was strong, with only a small degree of surface disintegration observed after prolonged sonication (Fig. S2 in the ESM). The elemental composition was analyzed using energy dispersive X-ray spectroscopy (EDS) and inductively coupled plasma atomic emission spectrophotometry (ICP-AES). As verified by EDS, the hollow spheres contained only Cu, Ce, and O elements, without other impurities (Fig. S3 in the ESM). The Ce/Cu atomic ratio determined by EDS and ICP-AES analyses was around 20:1, close to the feeding ratio of the Cu and Ce precursors. Additionally, both mapping and line-scan analyses of two microspheres revealed that big spheres and nanosheets contained only Cu, while the small particles decorating the surface were composed of Ce only, with oxygen being distributed over the whole sample.

The products collected before calcination were characterized by XRD. The obtained diffraction peaks were well-matched with those of the crystalline copper carbonate ($Cu_2(OH)_2CO_3$) and CeO_2 (Fig. S5(a) in the ESM). Compared to the non-calcined samples, the CeO_2-CuO samples exhibited no noticeable morphology changes after the decomposition process, as illustrated in Fig. S5(b) (in the ESM). However, high-magnification FESEM imaging (Fig. S5(c) in the ESM) reveals that calcination changed the dense structure of CuO nanorods into a highly porous structure composed of interconnected nanoparticles. Thermogravimetric analysis (TGA) of the non-calcined sample showed a weight loss of about 26% between 200 and 350 °C in air, well matching the theoretical value of 26.5% for the decomposition of $Cu_2(OH)_2CO_3$ to CuO (Fig. S5(d) in the ESM).

XPS provides information on the surface composition and electronic structure of samples. The XPS survey spectra of CeO_2-CuO verified the presence of Cu, Ce, O, and C elements (Fig. S6(a) in the ESM). The presence of C was ascribed to contamination during the test process. High-resolution XPS spectra showed that the Cu $2p_{3/2}$ and $2p_{1/2}$ peaks were located at binding energies of 934.1 and 953.9 eV, respectively, in accordance with the reported values for Cu^{2+} in the bulk phase (Fig. S6(b) in the ESM) [29]. Furthermore, the characteristic Cu^{2+} shake-up peaks at 940–945 eV were also clearly observed. The appearance of a weak peak at around 569.6 eV in the auger Cu LMM spectrum (AES) was attributed to Cu^+, indicating the reduction of a small portion of Cu^{2+} (Fig. S6(c) in the ESM). These results indicate that Cu^{2+} and Cu^+ coexisted in CeO_2-CuO samples. The presence of Cu^+ in CuO was reported to suggest the formation of oxygen vacancies [30]. In the high-resolution Ce 3d XPS spectrum, the six peaks marked as v (ca. 882.6 eV), v″ (ca. 889.0 eV), v‴ (ca. 898.5 eV), u (ca. 901.0 eV), u″ (ca. 907.7 eV), and u‴ (ca. 916.9 eV) were characteristic of Ce^{4+}, whereas the other two peaks labeled as v′ (ca. 885.1 eV) and u′ (ca. 903.6 eV) were indicative of Ce^{3+} species (Fig. S6(e) in the ESM) [31]. Thus, Ce mainly exists in the Ce^{4+} state due to the preparation conditions employed (calcination in air at 400 °C). The relative surface Ce^{3+} content with respect to the total amount of cerium species was as high as 22.3%, as determined by comparison of the corresponding XPS peak areas. These observations indicate a redox equilibrium ($Cu^{2+} + Ce^{3+} \leftrightarrow Cu^+ + Ce^{4+}$), which has been recognized as the source of the synergetic effect on catalyst reducibility [32–34]. As shown in Fig. S6(d) in the ESM, the high-resolution O 1s XPS spectrum reveals three types of oxygen species: The one with a binding energy at 529.9 eV is attributed to lattice oxygen bonded to metal ions, whereas the other two at 532.1 and 533.4 eV can be ascribed to the oxygen adsorbed on defects or chemically [30]. Compared to CuO, the binding energy of the peak at 529.9 eV in CeO_2-CuO is obviously shifted to a lower value, suggesting that the addition of CeO_2 reduces the binding energy between O and Cu ions, resulting in the facile reducibility of O species. Additionally, O_2 can be adsorbed onto the sample surface due to the presence of oxygen vacancies, producing species such as O_2^- ions.

It should be emphasized that our synthetic process is extremely simple and can be readily scaled up.

It has been demonstrated that ~5 g of products could be obtained using a 1,000-mL autoclave (Fig. S7 in the ESM).

The effects of several important parameters on the product synthesis, such as the type of precursor and solvent, hydrothermal reaction temperature and time, additives (including PVP and NaBr), and proportion of raw materials were systematically investigated. In the present synthesis, the selective use of acetate is critical for the formation of hollow spheres. When acetate was replaced with chloride, the reaction yielded aggregates composed of nanoparticles, which did not exhibit hollow structures (Fig. S8 in the ESM). Similarly, only irregular particles or solid microspheres were harvested when acetate was substituted with sulfate or nitrate (Figs. S9 and S10 in the ESM). To investigate the effect of solvent on product morphology, a series of control experiments were performed by varying the volume of EtOH or DMF introduced into the reaction system. Herein, the volume fraction of EtOH or DMF in the mixed EtOH–H_2O or DMF–H_2O solvent is defined as n. As shown in Figs. S11(a) and S11(b) in the ESM, when a low amount of EtOH was used (n = 25%), the obtained particles were composed of well-defined hollow microspheres with smaller CeO_2 particles attached to their surface, but the sizes of CuO spheres were relatively large (ca. 10 μm), with no nanosheets grown on their surface. If the volume fraction of EtOH was doubled (n = 50%), the resulting product consisted of only separate CuO and CeO_2 particles (Figs. S11(c) and S11(d) in the ESM). On the other hand, the hollow spheres prepared using DMF at n = 25 or 50% exhibited poor dispersity and tended to aggregate, as shown in Figs. S12(a)–S12(d) in the ESM. As the volume fraction of DMF was increased (n = 75%), the well-defined spheres could hardly be produced. Instead, heavily aggregated small CuO nanoparticles were obtained, with no obvious CeO_2-CuO heterostructures produced (Figs. S12(e) and S12(f) in the ESM). The lower dissolution rate of acetate in alcohols or DMF compared to that in water promotes the initial precipitation of solid spheres. Thus, the morphology variation of the product probably originates from the changes of diffusion and growth rates. These observations clearly suggest that solvent polarity plays an important role in the kinetically controlled synthesis of hierarchical hollow spheres with good monodispersity and well-defined shape.

The reaction temperature is another crucial parameter that significantly affects product morphology. When the hydrothermal reaction was carried out at 60 ℃, no CeO_2 particles were formed on the obtained solid CuO microspheres, possibly since CeO_2 was hardly crystallized at low temperatures (Figs. S13(a) and S13(b) in the ESM). As the reaction temperature was increased to 100 ℃, CeO_2 particles started to appear on the surface of CuO spheres, with the latter still having a solid core (Figs. S13(c) and S13(d) in the ESM). The formation of hollow CeO_2/CuO heterostructures was only observed at a higher temperature of 140 ℃. It is believed that the enhanced dissolution and diffusion rates of CO_3^{2-}, Cu^{2+}, and Ce^{3+} favor the quick reaction producing porous structures, while the product obtained at 180 ℃ comprises only bulk particles with irregular morphologies, probably resulting from the direct decomposition of precursor particles during hydrothermal synthesis (Figs. S13(e) and S13(f) in the ESM). The effect of additives was also examined. For example, the product mixture obtained in the presence of PVP contained a large fraction of irregular particles and few spheres (Figs. S14(a) and S14(b) in the ESM). However, the addition of inorganic salts such as NaBr to the synthetic mixtures increased both monodispersity and morphological yield (to nearly 100%). Furthermore, the obtained hollow spheres were entirely composed of nanosheets, as shown in Figs. S14(c) and S14(d) in the ESM.

The Ce/Cu precursor molar ratios (denoted as x) also significantly impact product morphology. Figure S15 in the ESM shows the morphology differences of the products obtained by tuning the initial compositions. When no Ce was introduced into the system, the obtained CuO showed a similar rambutan-like shape. Remarkably, rather long "thorns" were formed on the surface of the spheres (Fig. S15(a) in the ESM). Well-dispersed CeO_2-CuO hollow spheres could be prepared at $0 < x \leqslant 10\%$, as demonstrated by the FESEM images in Figs. S15(b)–S15(d) in the ESM, but the thorns on the surface exhibited different lengths, indicating that the Ce precursor can affect the growth of porous CuO microspheres. On the other hand, at higher x values (e.g., 20%), a physical mixture of CuO and

phase-separated CeO_2 was produced, suggesting that the addition of larger amounts of the $Ce(CH_3COO)_3$ precursor promotes spontaneous nucleation of Ce components, as verified by both SEM imaging and EDS mapping patterns (Figs. S15(e) and S15(f) in the ESM). UV–vis spectroscopic measurements also indicated the coexistence of CeO_2 and CuO in 2% CeO_2-CuO, 5% CeO_2-CuO, and 10% CeO_2-CuO samples, as shown in Fig. S16 in the ESM. The band at ca. 202 nm was attributed to the absorption of CuO, while the one at ca. 370 nm originated from the charge transfer between the O 2p and Ce 4f states in O^{2-} and Ce^{4+} [35].

To better understand the mechanism of hollow structure formation, a series of time-dependent experiments were performed, while maintaining all other experimental conditions identical to the ones shown in Fig. 1. Figures 3(a)–3(e) illustrate the morphological evolution of the particles with reaction time. Only small $Cu_2(OH)_2CO_3$ nanoparticles of ca. 30 nm size were obtained at an early reaction stage (15 min, not shown), due to the fast reaction of the large quantities of Cu^{2+} with the carbonate ions (CO_3^{2-}) and the hydroxide ions produced by hydrolysis of CO_3^{2-}. After a reaction time of 1 h, these unstable nanoparticles spontaneously assembled into solid microspheres with smooth surfaces, as shown in Fig. 3(a) and Fig. S17 in the ESM. The magnified FESEM image in Fig. 3(f) reveals that they were loosely packed. When the reaction duration was prolonged to 2 h, it was observed that the newly generated $Ce(OH)_3$ phase, which was easily converted to CeO_2 via oxidation–dehydration during the drying process, grew on the outer surface of pristine solid microspheres to form the heterostructure, as displayed in Fig. 3(b) and Fig. S18 in the ESM. It should be mentioned that the growth of CeO_2 particles occurred only on the surface of $Cu_2(OH)_2CO_3$ spheres but not in the bulk solution, which may be related to the specific surface properties of the $Cu_2(OH)_2CO_3$ crystal structures that were largely affected by the surrounding solvent. As the reaction proceeded (4 h), the structure continued to evolve: The small crystallites beneath the surface layer preferentially dissolved via the well-known inside-out Ostwald ripening process, leading to the formation of the unique hollow yolk/shell structure, as seen more clearly in the magnified image (Fig. 3(h) and Fig. S19 in the ESM). This is due to the fact that

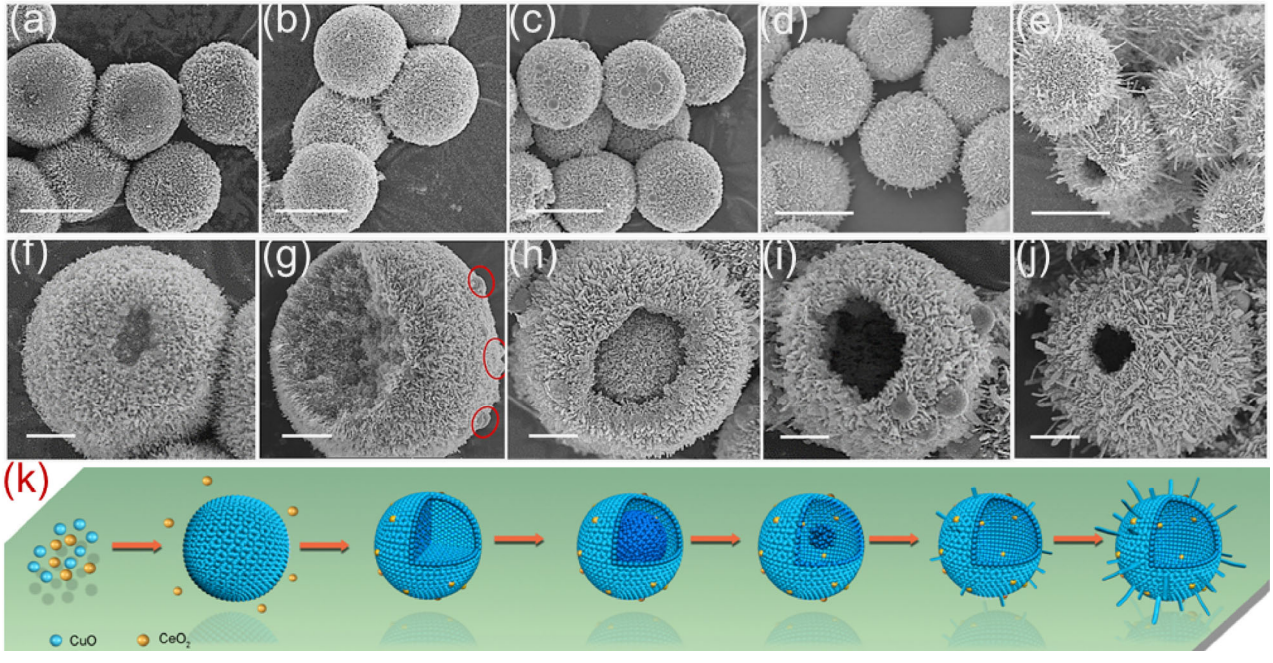

Figure 3 FESEM images of products collected after a reaction time of (a) and (f) 1, (b) and (g) 2, (c) and (h) 4, (d) and (i) 8, and (e) and (j) 12 h. Scale bars: 5 μm (low magnification) and 1 μm (high magnification). (k) Schematic illustration of the formation of hollow microspheres.

these small particles in interior regions possessed higher surface energies than those on the exterior surfaces. The gap between the core and the shell was estimated as ~1 μm. According to the report of Lou et al. on the template-free solvothermal synthesis of hollow SnO_2 nanospheres and the observations in this study, this evacuation process mainly depends on the packing of primary nanoparticles and the ripening characteristics of chemical species (e.g., solvent polarity or temperature). Moreover, it was also noticed that the primary nanoparticles on the outer surfaces became orderly arranged to form a rod-like structure, since they were easier to crystallize than those on the internal surface. When the reaction time was further extended to 8 h, the size of the inner core was decreased due to the minimization of surface energies until it vanished, producing a hollow structure stacked by nanorods. Meanwhile, the dissolved internal materials recrystallized to form small thin nanosheets, which gradually grew as "thorns" on the surface of these hollow spheres (Fig. 3(d) and Fig. S20 in the ESM). Eventually, after a 12-h reaction (Fig. 3(e) and Fig. S21 in the ESM), the original solid spheres evolved into well-defined rambutan-like hollow spheres with a rough surface, accompanied by the growth of nanosheets in both thickness and size. Afterwards, no further structural changes were observed for the product. A closer examination of Figs. 3(f)–3(j) reveals that the shell thickness did not obviously change with prolonged reaction time, but the particles diameter slightly increased, from ca. 5 to 6 μm, indicating the continuing evacuation of the internal core. Furthermore, the uniformity of microspheres was well preserved during the whole process. It is quite clear that crystallization of the primary particles and the hollowing process occurred simultaneously throughout the whole reaction (Fig. S22 in the ESM). Based on the above observations, the growth process of this unique hollow structure can be classified as "growth-cum-assembly Ostwald ripening", as schematically described in Fig. 3(k). Such a process is consistent with the previous report of Lou et al [17]. However, in the present study, no organic solvent was employed, but just pure water. Our investigation shows that the above hollowing process can be generalized to synthesize other metal oxide composites, such as ZnO-CuO, Mn_2O_3-CuO, and CoO-CuO. All of these structures were further confirmed by both XRD and EDS measurements (Figs. S23–S25 in the ESM).

N_2 adsorption–desorption measurements were employed to further characterize the porosity of the as-obtained heterostructures. As shown in Fig. S26 in the ESM, the observed type IV isotherms were characteristic of mesoporous materials. A high BET surface area of about 43.3 $m^2 \cdot g^{-1}$ with a broad pore distribution was observed, in agreement with the porous texture of the shell. Other samples, including solid CuO, solid CeO_2-CuO, and yolk–shell CeO_2-CuO were also tested. As shown in Table S1 in the ESM, the surface area and pore volume of the yolk–shell CeO_2-CuO sample were significantly reduced to 29.4 $m^2 \cdot g^{-1}$ and 0.11 $cm^3 \cdot g^{-1}$, respectively, consistent with the observation of a smaller hollow interior of these particles by TEM. The solid or non-hollow CeO_2-CuO sample exhibited a surface area of 27.2 $m^2 \cdot g^{-1}$ and a total pore volume of 0.081 $cm^3 \cdot g^{-1}$, slightly smaller than those of the yolk–shell CeO_2-CuO sample. As expected, the solid CuO sample showed the lowest surface area of only 17.1 $m^2 \cdot g^{-1}$ and the smallest total pore volume of 0.0075 $cm^3 \cdot g^{-1}$. As shown in Fig. S27 in the ESM, the Raman spectrum of pure CuO displays a main band around 290 cm^{-1}, related to the second-order transverse acoustic (2TA) [30]. After the introduction of cerium species, two additional bands around 463 and 580 cm^{-1} appeared. The former is attributed to the F_{2g} vibration mode of the CeO_2 lattice, while the latter can be ascribed to the presence of oxygen vacancies. For the hollow CeO_2-CuO sample, the F_{2g} vibration mode was weakened, broadened, and shifted to lower frequency, which is due to the synergistic interaction between CuO and CeO_2 via the abovementioned electron transfer ($Cu^{2+} + Ce^{3+} \leftrightarrow Cu^{+} + Ce^{4+}$) revealed by XPS measurements and the surface oxygen vacancies due to the existence of the reduced state of copper [30].

3.2 Electrochemical performance

In order to demonstrate the above structure-property relationship, all as-synthesized samples with different structures were tested as electrical capacitors (ECs). Figure 4 shows the representative cyclic voltammetry (CV) curves at different scan rates in a potential

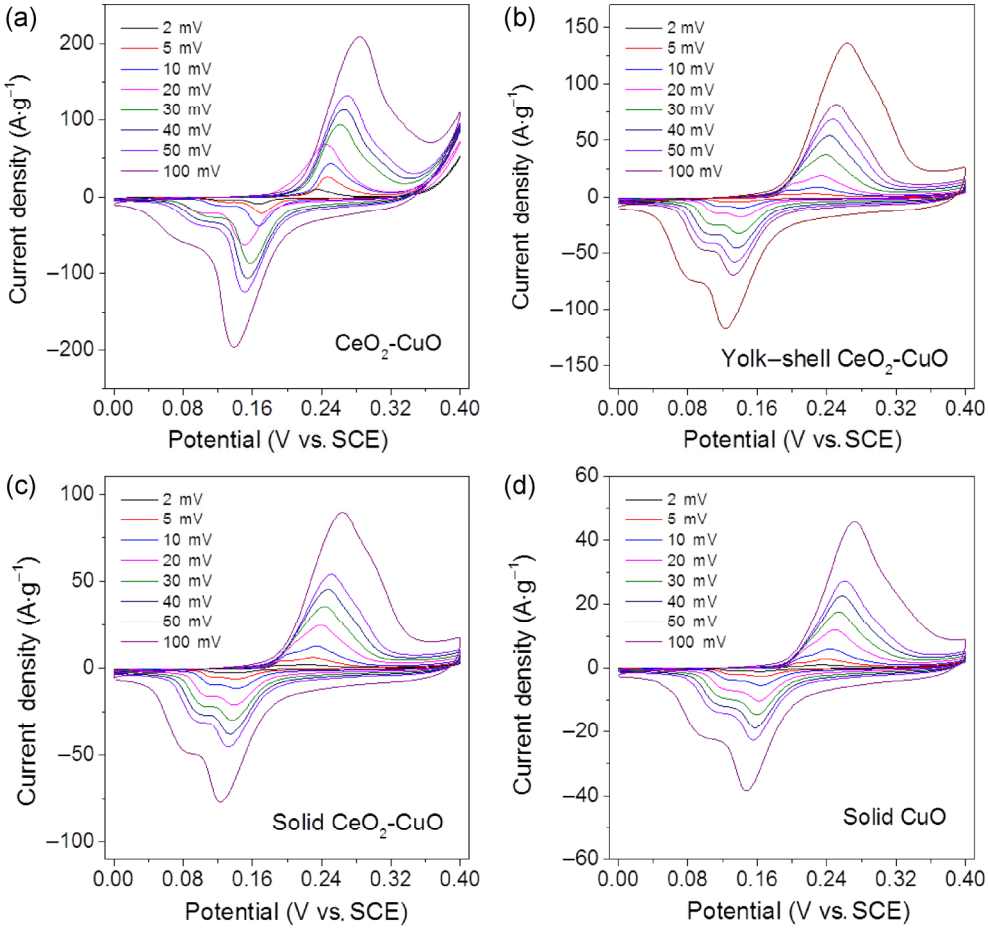

Figure 4 Comparative CV curves recorded at different scan rates for the electrodes.

window from 0 to 0.40 V vs. SCE. Well-defined redox peaks are visible in all CV curves as a result of the Faradic capacitive behavior of Cu^{+}/Cu^{2+} and Ce^{3+}/Ce^{4+}. The CV curve shapes did not significantly change with increased scan rate, except for a slight shift of the peak position, revealing the ideal capacitive behavior of all samples. The hollow CeO_2-CuO electrode exhibited the largest CV internal area, which decreased in the order of yolk–shell CeO_2-CuO, solid CeO_2-CuO, and solid CuO. This was mainly attributed to the higher surface area of the hollow CeO_2-CuO electrode that favors faster ionic transport in the electrodes. When the scan rate was increased, a lower specific capacitance was obtained for the electrodes due to the greater reduction of the effective ion–electrode interaction. Figure S28 in the ESM presents the galvanostatic charge–discharge voltage curves measured in a stable potential window between 0 and 0.32 V (vs. SCE) at various current densities, ranging from 1 to 5 $mA·g^{-1}$. The discharge time decreased with the change of microstructure, in agreement with the results of CV analysis. The as-synthesized hollow CeO_2-CuO electrode exhibited the longest discharge time (474 s), followed by the yolk–shell CeO_2-CuO (421 s), solid CeO_2-CuO (136 s), and solid CuO (84 s). As shown in Table S2 in the ESM, the hollow CeO_2-CuO electrode exhibits the highest capacitance at a given charge–discharge current density. For example, the maximum capacitance value of 698.4 $F·g^{-1}$ at a discharge current density of 1 $A·g^{-1}$ was achieved, which is higher than that of other previously reported electrode materials, such as single-component metal oxides, including CuO and Co_3O_4, and binary metal oxide composites (Table S3 in the ESM). The enhancement of electrochemical capacitance for the as-obtained CeO_2-CuO hollow sample is related to two factors: 1) Its larger

surface area causes a faster diffusion of ions from the electrolyte, which can enter almost all the effective electrode holes; 2) the coexistence of Ce^{4+} and Ce^{3+} due to the synergistic effect between CeO_2 and CuO influences the electrochemical reaction by altering the electron–hole pair recombination rate. It was reported that the electrochemical performance of CuO could also be improved by the addition of Co_2O_3, due to the synergistic effect of Co_2O_3 and CuO [36]. In addition, the Nyquist plots of the above samples are given in Fig. S29 in the ESM. The complex plane impedance plots of each sample can be divided into high-frequency and low-frequency components. The semicircle in the high-frequency range is associated with the surface properties of the porous electrode, which corresponds to the Faradic charge-transfer resistance. At lower frequencies, the straight sloping line represents the diffusive resistance (Warburg impedance) of the electrolyte in electrode pores and the proton diffusion in host materials. It can be seen that all samples have a small Faradic charge-transfer resistance, and the impedance of the hollow CeO_2-CuO electrode (0.357 Ω) is smaller than that of the other ones. Furthermore, the hollow CeO_2-CuO displays the highest phase angle at low frequencies, which may be attributed to its unique structural features. In addition, the electrochemical stabilities of these samples were investigated for 1,000 CV cycles at a scan rate of 200 $mV \cdot s^{-1}$, as shown in Fig. S30 in the ESM. The electrode capacity gradually decreases with increasing cycle numbers for all samples, but the CeO_2-CuO heterostructure exhibits a much slower decline rate than others. After 1,000 CV cycles, the capacity retention of CeO_2-CuO is still 92.1%, while those of the yolk–shell CeO_2-CuO, solid CeO_2-CuO, and solid CuO are only 81%, 70.4%, and 57.2%, respectively. This further confirms the superiority of this hierarchical hollow heterostructure.

3.3 Catalytic performance

It is anticipated that the larger specific surface area of the hollow CeO_2-CuO favors the uptake of gaseous reactants and could be beneficial for improving catalytic activity. The direct synthesis of methylchlorosilanes (MCSs) via the Rochow reaction, in which gaseous methyl chloride (MeCl) reacts with solid Si powder over Cu-based catalysts, is a very important process in organosilane industry [37, 38]. As shown in Scheme S1 in the ESM, this reaction produces various products, including M2, M1, M3, etc., with M2 being the most desirable one. To further confirm the structural superiority of the hollow microspheres, their catalytic properties toward the Rochow reaction were compared with those of hollow CuO, solid CeO_2, solid CuO, solid CuO-CeO_2, yolk–shell CeO_2-CuO, and commercial Cu-Cu_2O-CuO samples. Table S4 in the ESM summarizes the catalytic performance of all samples at 325 °C. As indicated therein, no activity is observed with pure solid CeO_2 as a catalyst. When using solid CuO under the same conditions, a Si conversion of 7.9% and an M2 selectivity of 63.6% are observed, suggesting that CuO is intrinsically active for this reaction. The hollow CuO shows a slightly higher performance (Si conversion of 11.5% and M2 selectivity of 70.6%), indicating the superiority of the hollow structure. However, the introduction of CeO_2 into CuO dramatically enhances the catalyst performance. The Si conversion and M2 selectivity are improved to 36.4% and 87.1%, respectively, for the hollow CeO_2-CuO sample, displaying an obvious synergistic effect. To clarify this issue further, a mechanical mixture of CeO_2 and hollow CuO at a molar ratio of 1:20 was used for comparison, showing a result similar to that of pure CuO. This fact indicates that simple physical mixing is unable to create effective interfacial contacts between the CuO and CeO_2 components, which appear to be crucial for enhanced properties. Other samples, including solid CeO_2-CuO, yolk–shell CeO_2-CuO, and solid CuO, also show performances inferior to that of the hollow CeO_2-CuO sample, further confirming the efficiency of the hollow structure. Specifically, solid CeO_2-CuO gives a Si conversion of 15.6% and an M2 selectivity of 75.1%, while the yolk–shell sample exhibits an M2 selectivity of 78.1% at 19.5% Si conversion. More importantly, the catalytic properties of the hollow CeO_2-CuO sample are even better than those of the commercial Cu-Cu_2O-CuO catalyst, although the latter has a more complex composition. These results clearly show that the as-prepared hollow CeO_2-CuO sample exhibits the best performance among all tested samples in terms of both M2 selectivity and Si conversion. In addition, the result achieved by CeO_2-CuO is also superior to those of most of the previously reported

Cu-based catalysts (Table S5 in the ESM). In terms of specific activity, i.e., turnover frequency (TOF), it is still the most active one for this reaction. Figure 5 further compares the catalytic behavior of as-obtained catalysts in the temperature range of 295–355 ˚C. It can be observed that for all samples, both Si conversion and M2 selectivity show a volcano-shape dependence on the reaction temperature, increasing between 295 and 325 ˚C and then dropping at higher temperatures. However, the hollow CeO_2-CuO catalyst still exhibits the highest activity at any given temperature. Besides the higher activity and selectivity, these hollow microspheres exhibit better stabilities than solid CeO_2-CuO under realistic conditions (0.1 MPa, 325 ˚C). Even when the reaction is continuously carried out for 72 h, this catalyst still maintains a stable M2 selectivity. In contrast, an obvious decay in M2 selectivity from 63.6% to 48.2% during 72 h of time-on-stream is observed for the solid CeO_2-CuO catalyst, accompanied by a marked selectivity increase of the undesired M1. In agreement with the excellent stability, TEM analysis shows no obvious morphology changes for the hollow CeO_2-CuO catalyst after 72 h of reaction (Fig. S31 in the ESM). Based on these observations, we speculate that the excellent properties of the hollow CeO_2-CuO sample are related to its unique assembled hollow spherical structure with numerous interior local heterostructures. On one hand, the nanostructured porous building blocks can offer more contact sites for solid Si, while the hollow structure may facilitate the diffusion of reactants/products, thus accelerating the reaction. On the other hand, the heterostructures can generate synergistic effects between the two metal oxide components. Our recent work has also revealed this synergistic effect in the CeO_2-CuO composite [39]. Last but not least, these hollow self-assembled

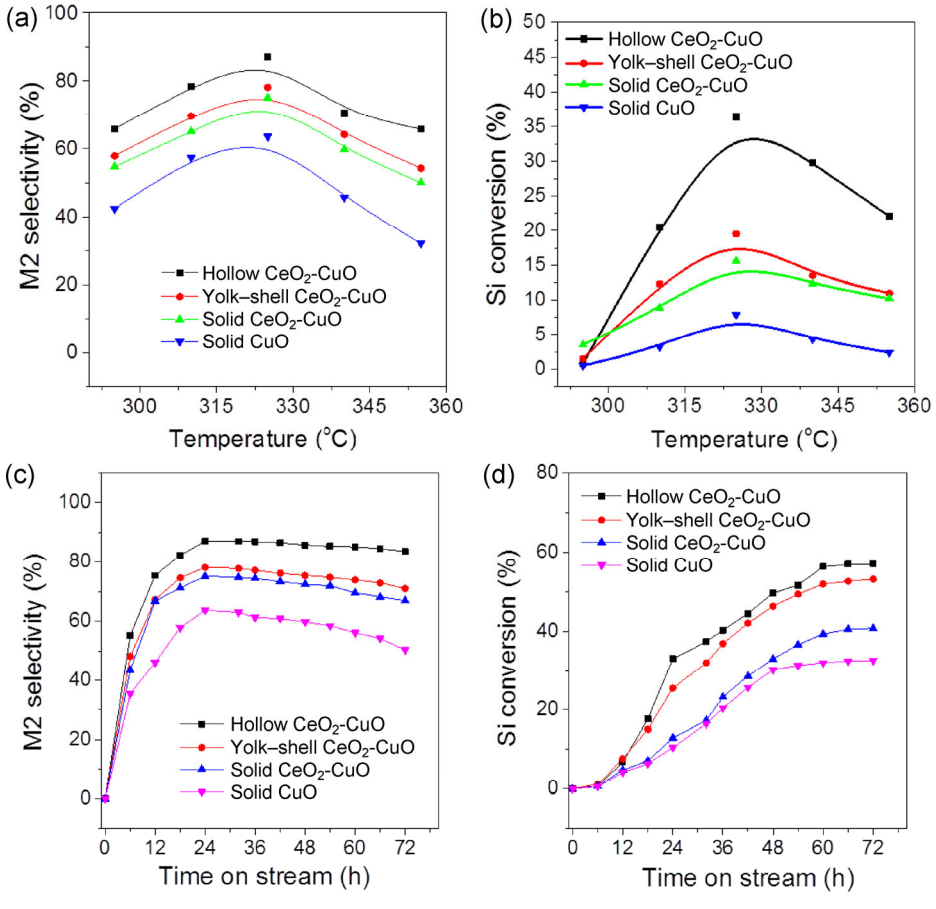

Figure 5 Dependence of (a) M2 selectivity and (b) Si conversion on the samples at different temperatures. Reaction conditions: T = 295–345 ˚C; others, see Table S3 in the ESM. Stability test for all samples: (c) M2 selectivity and (d) Si conversion. Reaction conditions: see Table S3 in the ESM.

microspheres exhibit a higher structural integrity and stability.

Previous literature reports showed that the Cu_xSi species generated during the reaction are must-have active intermediates in the synthesis of M2, with the formation of the active Cu_xSi species being the crucial step [40–44]. As demonstrated by the AES characterization above, the hollow CeO_2-CuO sample has a higher concentration of coordinatively unsaturated Cu^+, which may be due to the facile electron transfer between copper and ceria resulting from their intimate contact and small crystallite size ($Cu^{2+} + Ce^{3+} \leftrightarrow Cu^+ + Ce^{4+}$). Furthermore, the presence of Ce species stabilizes the surface Cu^+ ions that are locally coordinated to three oxygen atoms. Typical reports have disclosed that these low-coordinated atoms can reduce the activation energy of some catalytic reactions [45–49]. Hence, in the present system, compared with CuO, the larger number of defect sites (Cu^+, where oxygen species are active) in CeO_2-CuO most likely result in the lower activation energy of alloying between Si and Cu reduced by CH_3Cl (Fig. S32 in the ESM), thus forming a larger amount of Cu_xSi species. Regeneration of Cu^+ sites can be achieved via reduction by Ce^{3+} following the above equation. However, the overly rapid reduction of CuO causes the deposition of excess copper on the surface of the Cu-Si alloy, leading to side reactions. Indeed, an enlarged view of the XRD patterns for the used contact masses clearly indicates that the hollow CeO_2-CuO catalyst has a higher intensity of Cu_xSi species than other samples (Fig. S33 in the ESM). The EDS mapping pattern of the reacted contact masses shows the distribution of Si and Cu, clearly revealing the reacted (dark pink) and unreacted regions (bright pink) of Si particles, as well as the uniform distribution of elemental Cu in the reacted zone (Fig. S34 in the ESM). After removal of metallic Cu by ammonia washing, the residues were characterized by EDS mapping. As shown in Fig. S35 in the ESM, the predominant appearance of Cu in pits (reacted region) clearly indicated the existence of Cu_3Si. These observations demonstrate that the reaction proceeds via the formation of an intermediate. From the above analysis, a mechanism for the Rochow reaction catalyzed by the hollow structure was proposed, illustrated in Fig. 6. First, the Cu-based catalyst is mixed with Si to form the contact mass. As the reaction temperature increases, the catalyst reacts with CH_3Cl to form Cu* (highly active species), which then gradually diffuses into the Si matrix, accompanied by the formation of the active Cu_xSi alloy phase with cleaved Si* at the interface. The as-formed Cu_xSi species therein may exhibit modest adsorption and activation energies toward MeCl, which is subsequently transformed into M2. XPS evidence suggests that the Cu–O bond in CeO_2-CuO is weakened. Furthermore, as mentioned

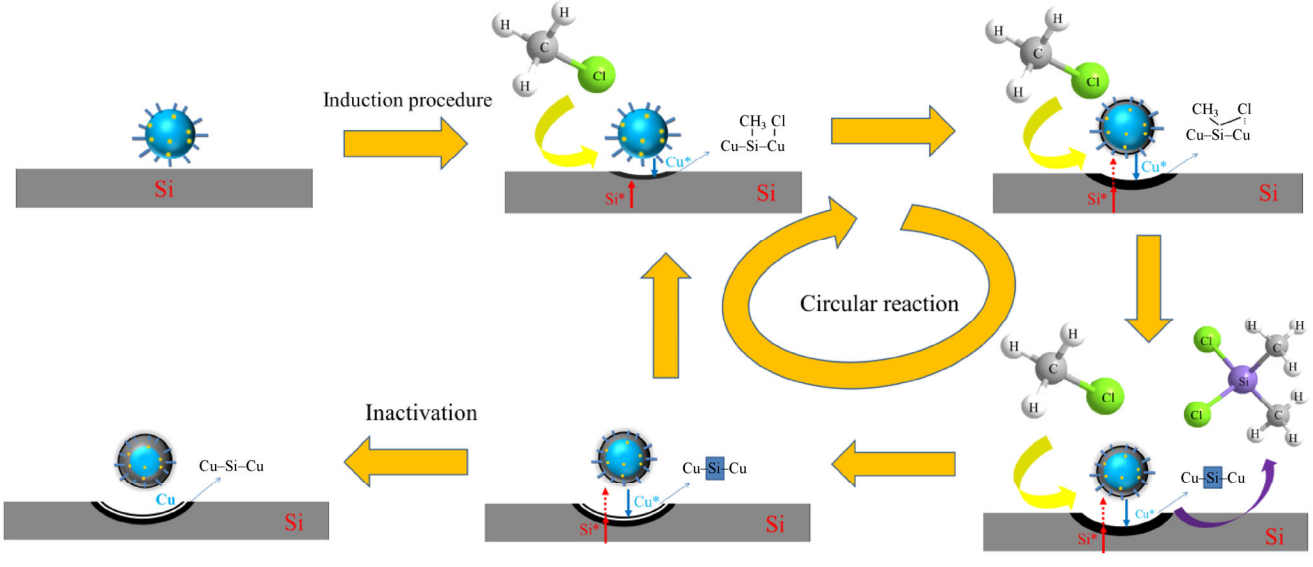

Figure 6 Schematic illustration of the mechanism proposed for the Rochow reaction.

above, the CeO_2-CuO composite exhibits a notable synergetic effect between CeO_2 and CuO, which facilitates interfacial charge transfer to form a larger number of surface defects (Cu^+ and oxygen vacancies), thus promoting the formation of the Cu-Si alloy and leading to enhanced activity. In addition, the hierarchical architecture enhances structural integrity and leads to high stability. As the reaction proceeds, more elemental copper is produced, while Cu in the Cu_xSi alloy is reduced until deactivated.

4 Conclusions

In summary, heterostructured CeO_2-CuO hollow microspheres have been successfully synthesized using a facile template-free hydrothermal route followed by calcination. The resulting CeO_2-CuO composite has a rambutan-like morphology, with spherical CeO_2 particles embedded in the walls of the prickly CuO hollow microspheres. The latter is primarily built up from interconnected CuO nanoparticles and the CuO nanorods assembled above the nanoparticle layer. Due to the advanced structure and the synergistic interaction between CuO and CeO_2, these hollow microspheres show a greatly enhanced capacity when used as supercapacitor and a superior catalytic activity in the Rochow reaction, as compared with their non-hollow and individual counterparts. Moreover, preliminary results show that this method is applicable to constructing other complicated structures containing multiple metal oxide components. This work demonstrates the first facile and scalable preparation of multi-component hollow metal oxides spheres with numerous interior heterostructures, achieved by a simple "bottom-up" hydrothermal reaction without the use of templates. Research of some other important applications of this type of materials is still underway.

Acknowledgements

The authors gratefully acknowledge the financial supports from the National Natural Science Foundation of China (Nos. 21506224, and 51272252). Z. Y. Z. would like to thank ICES for the kind support of the collaboration.

Electronic Supplementary Material: Supplementary material (detailed characterizations of CeO_2-CuO hollow microsphere as well as details of electrochemical and catalytic properties) is available in the online version of this article at http://dx.doi.org/10.1007/s12274-016-1298-0.

References

[1] Yin, Y. D.; Rioux, R. M.; Erdonmez, C. K.; Hughes, S.; Somorjai, G. A.; Alivisatos, A. P. Formation of hollow nanocrystals through the nanoscale Kirkendall effect. *Science* **2004**, *304*, 711–714.

[2] Gonzalez, E.; Arbiol, J.; Puntes, V. F. Carving at the nanoscale: Sequential galvanic exchange and Kirkendall growth at room temperature. *Science* **2011**, *334*, 1377–1380.

[3] Pan, X. L.; Fan, Z. L.; Chen, W.; Ding, Y. J.; Luo, H. Y.; Bao, X. H. Enhanced ethanol production inside carbon-nanotube reactors containing catalytic particles. *Nat. Mater.* **2007**, *6*, 507–511.

[4] Ameloot, R.; Vermoortele, F.; Vanhove, W.; Roeffaers, M. B. J.; Sels, B. F.; De Vos, D. E. Interfacial synthesis of hollow metal–organic framework capsules demonstrating selective permeability. *Nat. Chem.* **2011**, *3*, 382–387.

[5] Lou, X. W.; Archer, L. A.; Yang, Z. C. Hollow micro-/nanostructures: Synthesis and applications. *Adv. Mater.* **2008**, *20*, 3987–4019.

[6] Wang, Z. Y.; Zhou, L.; Lou, X. W. Metal oxide hollow nanostructures for lithium-ion batteries. *Adv. Mater.* **2012**, *24*, 1903–1911.

[7] Hu, J.; Chen, M.; Fang, X. S.; Wu, L. M. Fabrication and application of inorganic hollow spheres. *Chem. Soc. Rev.* **2011**, *40*, 5472–5491.

[8] Lai, X. Y.; Halpert, J. E.; Wang, D. Recent advances in micro-/nano-structured hollow spheres for energy applications: From simple to complex systems. *Energy Environ. Sci.* **2012**, *5*, 5604–5618.

[9] Yu, L.; Wu, H. B.; Lou, X. W. Mesoporous $Li_4Ti_5O_{12}$ hollow spheres with enhanced lithium storage capability. *Adv. Mater.* **2013**, *25*, 2296–2300.

[10] Wang, Z.; Jia, W.; Jiang, M. L.; Chen, C.; Li, Y. D. One-step accurate synthesis of shell controllable $CoFe_2O_4$ hollow microspheres as high-performance electrode materials in supercapacitor. *Nano Res.* **2016**, *9*, 2026–2033.

[11] Ibáñez, M.; Cabot, A. All change for nanocrystals. *Science* **2013**, *340*, 935–936.

[12] Zhang, L.; Wu, H. B.; Lou, X. W. Metal-organic-frameworks-derived general formation of hollow structures with high complexity. *J. Am. Chem. Soc.* **2013**, *135*, 10664–10672.

[13] Nai, J. W.; Tian, Y.; Guan, X.; Guo, L. Pearson's principle inspired generalized strategy for the fabrication of metal hydroxide and oxide nanocages. *J. Am. Chem. Soc.* **2013**, *135*, 16082–16091.

[14] Caruso, F.; Caruso, R. A.; Möhwald, H. Nanoengineering of inorganic and hybrid hollow spheres by colloidal templating. *Science* **1998**, *282*, 1111–1114.

[15] Kim, S. W.; Kim, M.; Lee, W. Y.; Hyeon, T. Fabrication of hollow palladium spheres and their successful application to the recyclable heterogeneous catalyst for Suzuki coupling reactions. *J. Am. Chem. Soc.* **2002**, *124*, 7642–7943.

[16] Pan, A. Q.; Wu, H. B.; Yu, L.; Lou, X. W. Template-free synthesis of VO_2 hollow microspheres with various interiors and their conversion into V_2O_5 for lithium-ion batteries. *Angew. Chem., Int. Ed.* **2013**, *52*, 2226–2230.

[17] Lou, X. W.; Wang, Y.; Yuan, C. L.; Lee, J. Y.; Archer, L. A. Template-free synthesis of SnO_2 hollow nanostructures with high lithium storage capacity. *Adv. Mater.* **2006**, *18*, 2325–2329.

[18] Ding, Y.; Xia, X.; Chen, W. C.; Hu, L. H.; Mo, L.; Huang, Y.; Dai, S. Y. Inside-out Ostwald ripening: A facile process towards synthesizing anatase TiO_2 microspheres for high-efficiency dye-sensitized solar cells. *Nano Res.* **2016**, *9*, 1891–1903.

[19] Wang, X.; Wu, X. L.; Guo, Y. G.; Zhong, Y. T.; Cao, X. Q.; Ma, Y.; Yao, J. N. Synthesis and lithium storage properties of Co_3O_4 nanosheet-assembled multishelled hollow spheres. *Adv. Funct. Mater.* **2010**, *20*, 1680–1686.

[20] Wang, B.; Wu, H. B.; Zhang, L.; Lou, X. W. Self-supported construction of uniform Fe_3O_4 hollow microspheres from nanoplate building blocks. *Angew. Chem., Int. Ed.* **2013**, *52*, 4165–4168.

[21] Ma, F. X.; Hu, H.; Wu, H. B.; Xu, C. Y.; Xu, Z. C.; Zhen, L.; Lou, X. W. Formation of uniform Fe_3O_4 hollow spheres organized by ultrathin nanosheets and their excellent lithium storage properties. *Adv. Mater.* **2015**, *27*, 4097–4101.

[22] Carreon, M. A.; Guliants, V. V. Ordered meso- and macroporous binary and mixed metal oxides. *Eur. J. Inorg. Chem.* **2005**, *2005*, 27–43.

[23] Morris, C. A.; Anderson, M. L.; Stroud, R. M.; Merzbacher, C. I.; Rolison, D. R. Silica sol as a nanoglue: Flexible synthesis of composite aerogels. *Science* **1999**, *284*, 622–624.

[24] Zeng, M.; Li, Y. Z.; Mao, M. Y.; Bai, J. L.; Ren, L.; Zhao, X. J. Synergetic effect between photocatalysis on TiO_2 and thermocatalysis on CeO_2 for gas-phase oxidation of benzene on TiO_2/CeO_2 nanocomposites. *ACS Catal.* **2015**, *5*, 3278–3286.

[25] Warule, S. S.; Chaudhari, N. S.; Kale, B. B.; Patil, K. R.; Koinkar, P. M.; More, M. A.; Murakami, R. Organization of cubic CeO_2 nanoparticles on the edges of self assembled tapered ZnO nanorods via a template free one-pot synthesis: significant cathodoluminescence and field emission properties. *J. Mater. Chem.* **2012**, *22*, 8887–8895.

[26] Hornés, A.; Hungría, A. B.; Bera, P.; López Cámara, A.; Fernández-García, M.; Martínez-Arias, A.; Barrio, L.; Estrella, M.; Zhou, G.; Fonseca, J. J. et al. Inverse CeO_2/CuO catalyst as an alternative to classical direct configurations for preferential oxidation of CO in hydrogen-rich stream. *J. Am. Chem. Soc.* **2010**, *132*, 34–35.

[27] López Cámara, A.; Cortés Corberán, V.; Barrio, L.; Zhou, G.; Si, R.; Hanson, J. C.; Monte, M.; Conesa, J. C.; Rodriguez, J. A.; Martínez-Arias, A. Improving the CO-PROX performance of inverse CeO_2/CuO catalysts: Doping of the CuO component with Zn. *J. Phys. Chem. C* **2014**, *118*, 9030–9041.

[28] Yen, H.; Seo, Y.; Kaliaguine, S.; Kleitz, F. Tailored mesostructured copper/ceria catalysts with enhanced performance for preferential oxidation of CO at low temperature. *Angew. Chem., Int. Ed.* **2012**, *51*, 12032–12035.

[29] Liu, P.; Hensen, E. J. M. Highly efficient and robust Au/$MgCuCr_2O_4$ catalyst for gas-phase oxidation of ethanol to acetaldehyde. *J. Am. Chem. Soc.* **2013**, *135*, 14032–14035.

[30] Ma, J. H.; Jin, G. Z.; Gao, J. B.; Li, Y. Y.; Dong, L. H.; Huang, M. N.; Huang, Q. Q.; Li, B. Catalytic effect of two-phase intergrowth and coexistence CuO–CeO_2. *J. Mater. Chem. A* **2015**, *3*, 24358–24370.

[31] Liu, X. W.; Zhou, K. B.; Wang, L.; Wang, B. Y.; Li, Y. D. Oxygen vacancy clusters promoting reducibility and activity of ceria nanorods. *J. Am. Chem. Soc.* **2009**, *131*, 3140–3141.

[32] Avgouropoulos, G.; Ioannides, T. Effect of synthesis parameters on catalytic properties of CuO-CeO_2. *Appl. Catal. B: Environ.* **2006**, *67*, 1–11.

[33] Polster, C. S.; Nair, H.; Baertsch, C. D. Study of active sites and mechanism responsible for highly selective CO oxidation in H_2 rich atmospheres on a mixed Cu and Ce oxide catalyst. *J. Catal.* **2009**, *266*, 308–319.

[34] Kydd, R.; Teoh, W. Y.; Wong, K.; Wang, Y.; Scott, J.; Zeng, Q.-H.; Yu, A.-B.; Zou, J.; Amal, R. Flame-synthesized ceria-supported copper dimers for preferential oxidation of CO. *Adv. Funct. Mater.* **2009**, *19*, 369–377.

[35] Li, Z. Q.; Wang, H. L.; Zi, L. Y.; Zhang, J. J.; Zhang, Y. S. Preparation and photocatalytic performance of magnetic TiO_2-Fe_3O_4/graphene (RGO) composites under VIS-light irradiation. *Ceram. Int.* **2015**, *41*, 10634–10643.

[36] Shanmugavani, A. L.; Selvan, R. K. Improved electrochemical performances of $CuCo_2O_4$/CuO nanocomposites for asymmetric supercapacitors. *Electrochim. Acta* **2016**, *188*, 852–862.

[37] Hurd, D.T.; Rochow, E.G. On the mechanism of the

reaction between methyl chloride and silicon-copper. *J. Am. Chem. Soc.* **1945**, *67*, 1057–1059.

[38] Rochow, E.G. The direct synthesis of organosilicon compounds. *J. Am. Chem. Soc.* **1945**, *67*, 963–965.

[39] Jin, Z. Y.; Li, J.; Shi, L. S.; Ji, Y. J.; Zhong, Z. Y.; Su, F. B. One-pot hydrothermal growth of raspberry-like CeO_2 on CuO microsphere as copper-based catalyst for Rochow reaction. *Appl. Sur. Sci.* **2015**, *359*, 120–129.

[40] Ward, W. J.; Ritzer, A.; Carroll, K. M.; Flock, J. W. Catalysis of the Rochow direct process. *J. Catal.* **1986**, *100*, 240–249.

[41] Floquet, N.; Yilmaz, S.; Falconer, J. L. Interaction of copper catalysts and Si(100) for the direct synthesis of methylchlorosilanes. *J. Catal.* **1994**, *148*, 348–368.

[42] Luo, W. X.; Wang, G. R.; Wang, J. F. Effect of CuCl particle size on the reduction reaction by silicon in preparation of contact mass used for methylchlorosilane synthesis. *Ind. Eng. Chem. Res.* **2006**, *45*, 129–133.

[43] Somorjai, G. A.; Park, J. Y. Molecular factors of catalytic selectivity. *Angew. Chem., Int. Ed.* **2008**, *47*, 9212–228.

[44] Honkala, K.; Hellman, A.; Remediakis, I. N.; Logadottir, A.; Carlsson, A.; Dahl, S.; Christensen, C. H.; Nørskov, J. K. Ammonia synthesis from first-principles calculations. *Science* **2005**, *307*, 555–558.

[45] Kwak, J. H.; Hu, J. Z.; Mei, D. H.; Yi, C. W.; Kim, D. H.; Peden, C. H. F.; Allard, L. F.; Szanyi, J. Coordinatively unsaturated Al^{3+} centers as binding sites for active catalyst phases of platinum on γ-Al_2O_3. *Science* **2009**, *325*, 1670–1673.

[46] Jaramillo, T. F.; Jørgensen, K. P.; Bonde, J.; Nielsen, J. H.; Horch, S.; Chorkendorff, I. Identification of active edge sites for electrochemical H_2 evolution from MoS_2 nanocatalysts. *Science* **2007**, *317*, 100–102.

[47] Fu, Q.; Li, W. X.; Yao, Y. X.; Liu, H. Y.; Su, H. Y.; Ma, D.; Gu, X. K.; Chen, L. M.; Wang, Z.; Zhang, H. et al. Interface-confined ferrous centers for catalytic oxidation. *Science* **2010**, *328*, 1141–1144.

[48] Zhao, Y. F.; Chen, G. B.; Bian, T.; Zhou, C.; Waterhouse, G. I. N.; Wu, L. Z.; Tung, C. H.; Smith, L. J.; O'Hare, D.; Zhang, T. R. Defect-rich ultrathin ZnAl-layered double hydroxide nanosheets for efficient photoreduction of CO_2 to CO with water. *Adv. Mater.* **2015**, *27*, 7824–7831.

[49] Rong, H. P.; Mao, J. J.; Xin, P. Y.; He, D. S.; Chen, Y. J.; Wang, D. S.; Niu, Z. Q.; Wu, Y. E.; Li, Y. D. Kinetically controlling surface structure to construct defect-rich intermetallic nanocrystals: Effective and stable catalysts. *Adv. Mater.* **2016**, *28*, 2540–2546.